ChemComm

Accepted Manuscript

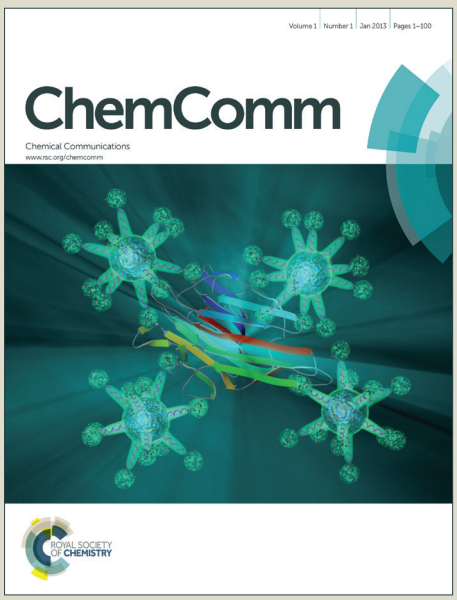

ROYAL SOCIETY OF CHEMISTRY

www.rsc.org/chemcomm

Journal Name

RSCPublishing

COMMUNICAITION

Co_3O_4 Nanoparticles Embedded Carbonaceous Fibre: Nanoconfinement Effect on Enhanced Lithium-Ion Storage

Cite this: DOI: 10.1039/x0xx00000x

Received 00th January 2012,
Accepted 00th January 2012

DOI: 10.1039/x0xx00000x

www.rsc.org/

Jin Sun [a], Daohao Li [a], Yanzhi Xia,*[,a] Xiaoyi Zhu [a], Lu Zong,[a] Quan Ji,[a] Yi (Alec) Jia,[b] Dongjiang Yang,*[,a,b]

Co_3O_4 nanoparticles embedded carbonaceous fibres were prepared from Co^{2+} coordinated regenerated cellulose fibres, which showed a high reversible capacity and excellent cycling stability as anode materials for Li-ion batteries.

Rechargeable lithium-ion batteries (LIBs) have long been considered as most promising reversible energy storage for a wide variety of application.[1] Graphite has been extensively applied as anode material for commercial LIBs because of their low cost and good stability. However, a theoretical capacity of only 372 mAh g^{-1} significantly limits its LIBs performance.[2] Although transition metal oxides (TMOs) are promising alternatives for high-performance LIBs anode materials because of their high theoretical capacities, they suffer from the problems of poor electronic conductivity and a large volume change during charge/discharge process, resulting in poor cycling performance.[3] To address the drawbacks of the TMOs anodes, one approach is to develop nanostructure TMOs/carbon composites,[4] where the nanoconfinement effect of carbon matrix can efficiently alleviate the aggregation and mechanical strain generated by repeated volume expansion/contraction of TMOs nanoparticles (NPs) and enhance the electrochemical conductivity. For instance, the confinement of SnO_2 NPs inside few-walled carbon nanotubes can contribute to an excellent cycling performance since the volume restriction inside carbon nanotubes can efficiently inhibit breakage during lithium insertion/extraction.[5] However, the traditional strategies to prepare these composites need either complicated synthesis or relatively high cost. The simple processes towards scaling up production of TMOs/carbon anodes are still highly desirable.

Cellulose is a linear homopolymer with high molecular weight composed of b-D-glucopyranose units connected through β-(1-4) linkages, which is a key source of sustainable and non-toxicity materials.[6] It is a green strategy to produce highly functionalized carbonaceous materials by means of the thermal or hydrothermal carbonization of cellulose.[7, 8] Cellulose could be modified and functionalized to carboxymethyl cellulose (CMC) directly by replacing the hydroxyl groups (–OH) groups with carboxymethyl ($–CH_2COO^-$) groups.[9] The negatively charged carboxylate ($–COO^-$) groups in the two adjacent chains of CMC or intra-macromolecular could coordinate with metal ions (M^{n+}), such as Co^{2+}, Ni^{2+}, and Fe^{3+}, to form M^{n+}-CMC through ion-exchange process, for the applications of biolabeling and flameresistant materials.[10-12] After pyrolysis of the M^{n+}-CMC in inert gas atmosphere, it is expected to obtain a TMOs NPs/carbon composite. In this communication, $–COO^-$ surface groups were firstly created on the regenerated cellulose microfibers (RCFs) to bind Co^{2+} cations (Co-RCFs). After heat treatment at 800 °C in N_2 and subsequent oxidation in air, the Co-RCFs converted to a novel nano/micro hierarchical structure in which Co_3O_4 NPs (~50-100 nm) were embedded in the surface of the carbonaceous fibres (Co_3O_4/CF-X, X denotes postoxidation time). The nanoconfinement effect on the Co_3O_4 NPs constrained by the carbonaceous fibre matrix could efficiently enhance the cycling performance.[13-15] So as expected, the composite anode shows a high reversible capacity of 730 mAh g^{-1} at 89 mA g^{-1} after 100 cycles as well as excellent rate capability. Apparently, this simple and environmentally friendly strategy is more feasible to synthesize a TMOs/carbon LIBs anode on a large scale compared with the conventional chemical vapor deposition and hydrothermal methods.

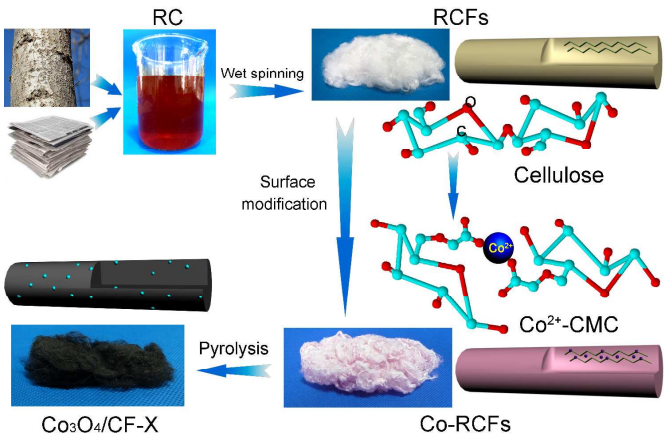

Scheme. 1 The synthesis of Co_3O_4/CF-X from surface modified RCFs.

As illustrated in Scheme 1, the synthesis of the Co_3O_4/CF-X samples was involved in a three-step process. Firstly, the RCFs were fabricated via wet-spinning technique by using the spinning dope of aqueous solution of RC and sodium hydroxide (NaOH) (Fig. S1). Secondly, the obtained RCFs were soaked and vibrated in NaOH/ethanol solution, and then chloroacetic acid ($ClCH_2COOH$) was added to convert the surface –OH of RCFs into $–CH_2COO^-$ via typical etherification reaction. The obtained surface modified RCFs were soaked in 5 wt% cobalt chloride ($CoCl_2$) ethanol solution to capture Co^{2+} cations electrostatically on the fibers (Co-RCFs), resulting in the white RCFs turn to light purple. The weight percentage of Co species in the Co-RCFs is determined to be about 2.17% by using thermogravimetric analysis (TGA) (Fig. S2). Finally, after calcination of 800 °C for 1 h in N_2 atmosphere and subsequent oxidation in air at 400 °C for 30, 60, and 90 min, the Co-RCFs converted to Co_3O_4/CF-X.

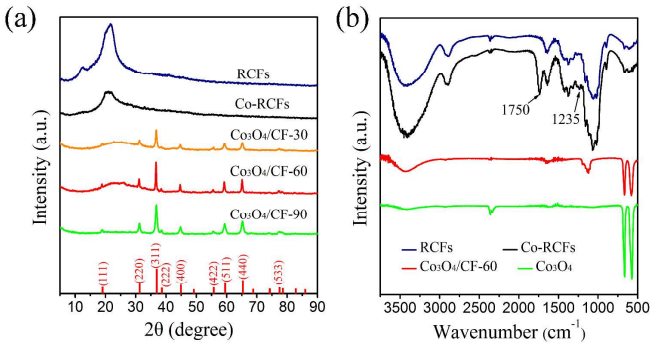

Fig. 1 (a) XRD patterns of RCF, Co-RCF, Co_3O_4/CF-30, Co_3O_4/CF-60, and Co_3O_4/CF-90. (b) FTIR spectra of the RCF, Co-RCF, Co_3O_4/CF-60, and commercial Co_3O_4.

Fig. 1a shows the X-ray diffraction (XRD) patterns of RCFs, Co-RCFs, and Co_3O_4/CF-X. RCFs have the typical XRD pattern of cellulose II at 2θ value of 12.1°, 20.1°, and 21.8°, and the crystalline polymorph of RCFs was formed during the wet-spinning process.[16] The same diffraction peaks are also observed from the diffraction pattern of the Co-RCFs, indicating the cellulose II structure of the fibres is maintained. After calcination in N_2 atmosphere and subsequent oxidation in air, the Co^{2+} cations completely convert to Co_3O_4 species. The strong and sharp diffraction peaks at 2θ values of 31.3, 36.9, 44.9, 59.5, and 65.3° are observed from the XRD pattern of Co_3O_4/CF-X samples, corresponding to the diffraction of (220), (311), (400), (511), and (440) planes of cubic crystalline Co_3O_4 (JCPDS No. 42-1467). The peak intensity increases with the extension of postoxidation time from 30 to 60 and 90 min. In addition, the broad diffraction peak of amorphous carbon (2θ=25.0°) is resulted from the pyrolysis of RCFs, which disappears after long time oxidation (Co_3O_4/CF-90). Fourier transformed infrared spectroscopy (FTIR) of the RCFs, Co-RCFs, Co_3O_4/CF-60, and commercial Co_3O_4 are displayed in Fig. 1b. For Co-RCFs, two characteristic peaks at 1750 and 1235 cm^{-1} are ascribed to the stretching vibration of C=O and COO^- ester functional groups,[17, 18] respectively, indicating that the surface of RCFs has been modified by etherification reaction. After pyrolysis and postoxidation, the Co-O stretching vibration bands of Co_3O_4 appear at 663 and 570 cm^{-1} in the spectrum of Co_3O_4/CF-60. The N_2 absorption-desorption isotherms and pore size distributions obtained from the Barrett–Joyner–Halenda (BJH) method are shown in Fig. S3. Co_3O_4/CF-60 exhibits a high specific surface area of 320 $m^2\ g^{-1}$, larger than those of Co_3O_4/CF-30 (214 $m^2\ g^{-1}$), and Co_3O_4/CF-90 (178 $m^2\ g^{-1}$). And Co_3O_4/CF-60 displays a multi-modal pore size distribution at 2.5, 9.0, and 63.2 nm. The high specific surface and porous structure could increase the contact of active material with electrolyte, shorten Li^+ diffusion path and thus improve the electrochemical performance.[19-21]

The morphology of the RCFs, Co-RCFs and Co_3O_4/CF-X was studied by field emission scanning electron microscope (FESEM). As shown in Fig. 2a, a single RCF is straight and smooth with a diameter of ~15 μm. After capture of Co^{2+} cations, the single Co-RCF possesses similar morphology with RCF (Fig. 2b), indicating that the introduction of the Co^{2+} cations does not influence the appearance of the fibres. After pyrolysis of Co-RCF in N_2 and oxidation in air, a large amount of Co_3O_4 NPs in the size range of ~50-100 nm are homogeneously embedded on the surface of the fibers (Fig. 2c and Fig. S4). The magnified SEM image of Co_3O_4/CF-60 in Fig. 2d shows the highly porous structure close to the Co_3O_4 NPs, which can serve as the electrolyte pathway to ensure good electrolyte immersion with the Co_3O_4 NPs (Fig. 2d). In addition, elemental mapping by energy dispersive X-ray spectroscopy (EDS) was used to analyse the distribution of the C, Co, and O elements in the fibre. As shown in Fig. 2e, homogeneously distributed C, Co, and O elements can be detected in a single fibre of Co_3O_4/CF-60.

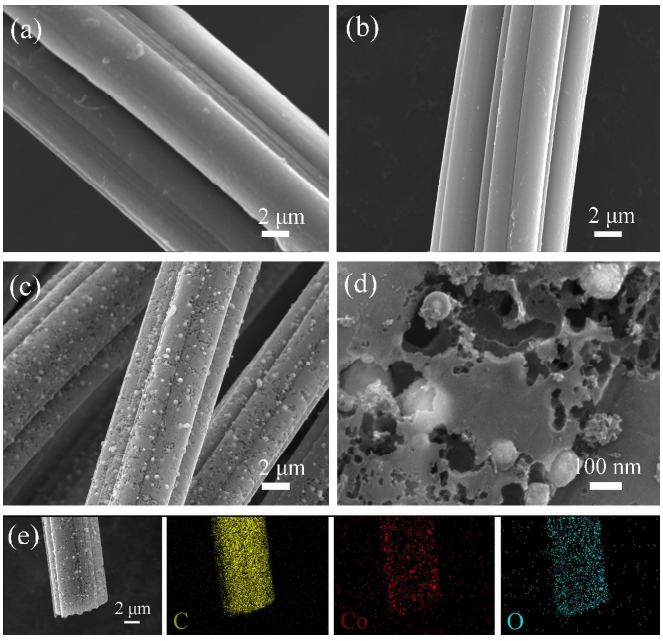

Fig. 2 SEM images of (a) RCF, (b) Co-RCF, (c, d) Co_3O_4/CF-60. (e) SEM image of Co_3O_4/CF-60 and corresponding EDS mapping for C, Co, O elements.

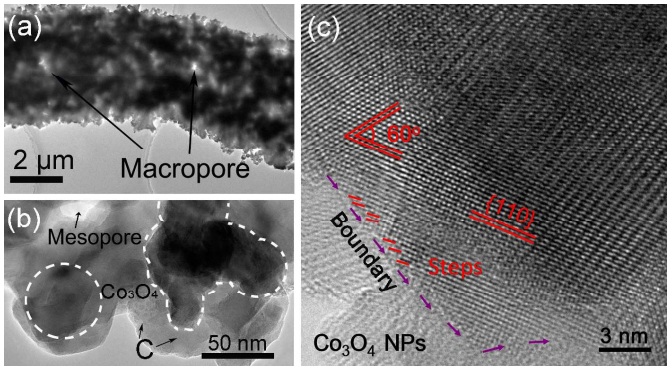

Fig. 3 (a) Low-magnification TEM, (b) high-magnification TEM, and (c) HRTEM image of Co_3O_4/CF-60.

Transmission electron microscope (TEM) and high-resolution TEM (HRTEM) images of Co_3O_4/CF-60 are presented in Fig. 3. As shown in Fig. 3a, a large number of Co_3O_4 NPs are distributed throughout a single fibre, and macropores are formed via the aggregation of large Co_3O_4 NPs. More importantly, it is notable that carbon matrix resulting from the carbonization of the $-CH_2COO^-$ groups is adjacent to the Co_3O_4 NPs (Fig. 3b), and such Co_3O_4 NPs-carbon nanoconfiment structure is efficient to increase the conductivity of the Co_3O_4 NPs and to counteract the pulverization of the Co_3O_4 NPs that takes place during charge/discharge cycles. Fig. 3c further shows a HRTEM image of the Co_3O_4 NPs. Apparently, the plane of {110} of cubic Co_3O_4 is exposed, which corresponds to the [011] zone-axis of Co_3O_4 NPs. The {110} plane has a high density of atomic steps which is helpful to enhance electrochemical performance.[22, 23]

Cyclic voltammetry (CV) and galvanostatic cycling analysis were used to examine the electrochemical properties of Co_3O_4/CF-X as LIBs anodes. Co_3O_4 exhibits high theoretical capacity according to reduction/oxidation reactions ($Co_3O_4+8Li^++8e^-\leftrightarrow 4Li_2O+3Co$). Fig. 4a shows the CV curves of Co_3O_4/CF-60 at a scan rate of 0.1 mV s^{-1}. In the first cathodic scan, two cathodic peaks were observed at 0.67 and 0.85 V, corresponding to the formation of solid-electrolyte-interphase (SEI) film and electrochemical reduction (lithiation) reaction of Co_3O_4 with Li^+. The broad anodic peak at 2.07 V can be ascribed to the oxidation (delithiation) reaction of Co_3O_4. In the second cycle, the main oxidation peak shifts to 2.18 V, and the cathodic peak is observed at 1.16 V. The peak intensity and integral areas of the third cycle are close to that of the second one for Co_3O_4/CF-60, indicating the electrochemical reversibility is gradually built after the initial cycle. Fig. 4b shows the charge/discharge curves of the Co_3O_4/CF-60 at 89 mA g^{-1} in the voltage range of 0.01−3.0 V (*vs.* Li^+/Li) at the 1st, 2nd, 50th and 100th cycle, respectively. The first discharge and charge specific capacities of Co_3O_4/CF-60 are 1246 and 733 mAh g^{-1} with a Coulombic efficiency (CE) of 58.8%. The restricted CE during the first cycle is assigned to the decomposition of electrolyte, forming a SEI on the electrode surface, and to the irreversible insertion of Li ions into pores of the fibers. Nevertheless, the CE value rises to 99.1% in the fifth

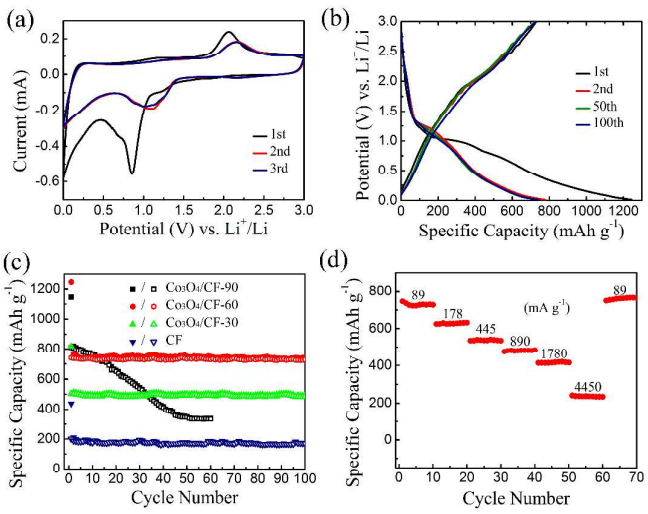

Fig. 4 (a) CV curves of Co_3O_4/CF-60. (b) The Co_3O_4/CF-60 cycled at the 1st, 2nd, 50th, and 100th between 0.01 and 3.0 V (*vs.* Li^+/Li) at a current density of 89 mA g^{-1}. (c) Comparison of the cycling performance of Co_3O_4/CF-30, Co_3O_4/CF-60, Co_3O_4/CF-90, and the pure CF. (d) The reversible specific capacity of the Co_3O_4/CF-60 at different rates.

cycle and then remains above 98% in the following cycles (as shown in Fig. S5). In addition, after 50th and 100th charge/discharge cycles, it exhibits a high reversible capacity of ~730 mAh g^{-1}, indicating good cycling stability.

The electrochemical performance of the Co_3O_4/CF-60 was compared with Co_3O_4/CF-30, Co_3O_4/CF-90, pure CF obtained by pyrolysis of RCF, and commercial Co_3O_4. As shown in Fig. 4c, Co_3O_4/CF-60 exhibits a high reversible specific capacity of 730 mAh g^{-1} at 89 mA g^{-1} after 100 cycles. This value is much higher than those of Co_3O_4/CF-30 (496 mAh g^{-1}) and pure CF (170 mAh g^{-1}). For Co_3O_4/CF-90 and commercial Co_3O_4 electrodes, their specific capacities fades seriously after 50 cycles (Fig. 4c and S6), although they exhibits high capacities at the initial stage. The best electrochemical performance of the Co_3O_4/CF-60 electrode results from the optimal content of carbon in the composite which is able to simultaneously insure both high specific capacity and cycling stability. As shown in Fig. S7, about 75.8, 32.1, and 9.9 % mass ratio of carbon are remained in Co_3O_4/CF-30 Co_3O_4/CF-60, and Co_3O_4/CF-90 after postoxidation, respectively.

The Co_3O_4/CF-60 electrode also exhibits the specific capacities of 632, 540, 484, 420, and 240 mAh g^{-1} at 178, 445, 890, 1780, to 4450 mA g^{-1}, respectively, indicating excellent cycling performance (Fig. 4d). In addition, a reversible capacity of 750 mAh g^{-1} was recovered, when the current density is decreased to 89 mA g^{-1}. This indicates that the integrity of the fibrous electrode has been preserved even after experiencing high rate charge/discharge. As shown in Fig. S8, there is no obvious change in morphology of the Co_3O_4/CF-60 electrode before and after 100 galvanostatic charge-discharge cycles. We also compared the electrochemical performance of the Co_3O_4/CF-60 electrode with the reported Co_3O_4/carbon composite electrodes[24,25] (Fig. S9). Besides the high specific

capacity, the Co_3O_4/CF-60 electrode displays better cycling performance.

The high reversible specific capacity, excellent cycling stability and rate performance should be attributed to the nanoconfinement effect on the embedded Co_3O_4 NPs by the carbonaceous fibre matrix. First, the unique one dimensional carbonaceous fibre matrix is employed as effective "matrix" material to release the mechanical strain induced during Li^+ charge/discharge process and prevent the aggregation of Co_3O_4 NPs, and can serve as the channels for fast electron transport to improve the electronic transport, thus enhance the cycle and rate performance. Second, the macropores and mesopores in the carbonaceous fibre can store the electrolyte as the "reservoirs" to increase the interface between active materials and electrolyte, thus shortening the diffusion distance of Li ions.[26-28]

In summary, we have prepared novel Co_3O_4/Carbon fibres by simple pyrolysis of wetspun modified cobalt cellulose fibres. The composite possesses the unique hierarchical microstructure in which Co_3O_4 NPs are embedded in micro-sized carbonaceous fibrous matrix and exhibits excellent electrochemical performance when used as an anode for Li-ion batteries. Co_3O_4/CF-60 obtained under the optimum conditions (oxidized with 60 min) exhibits high initial reversible specific capacity, excellent cycling stability, ie. 730 mAh g^{-1} after 100 cycles at 89 mA g^{-1}, and good rate performance. The excellent electrochemical performance is attribute to its unique nanoconfinement structure where the synergistic effect of Co_3O_4 NPs and bifunctional carbon fibre matrix (confining scaffold and conducting network), which greatly enhances the reversible capacity, cycling stability and rate performance. This work may pave a new way for scalable synthesis of nanoconfined TMO/Carbon anode materials.

This work was financially supported by the National Natural Science Foundation of China (50673046), the Basic application research plan of Qingdao City (11-2-4-2-(15)-jch), and ARC Discovery Project (No.130104759).

Notes and references

[a]Collaborative Innovation Centre for Marine Biomass Fibres, Materials and Textiles of Shandong Province; College of Chemical and Environmental Engineering, Qingdao University, Qingdao, P. R. China. E-mail: xiayzh@qdu.edu.cn

[b]Queensland Micro- and Nanotechnology Centre (QMNC), Griffith University, Nathan, Brisbane, Queensland 4111, Australia. E-mail: d.yang@griffith.edu.au.

†Electronic Supplementary Information (ESI) available. Experimental Section, wet spinning process, SEM images of Co_3O_4/CF-30 and Co_3O_4/CF-90, N_2 adsorption-desorption isotherms and BJH pore size distribution analysis, TGA measurement, and electrochemical properties of commercial Co_3O_4 electrodes. See DOI: 10.1039/b000000x/.

1. S. Megahed and B. Scrosati, *J. Power Sources*, 1994, **51**, 79-104.
2. Y. P. Wu, E. Rahm and R. Holze, *J. Power Sources*, 2003, **114**, 228-236.
3. L. Zhuo, Y. Wu, J. Ming, L. Wang, Y. Yu, X. Zhang and F. Zhao, *J. Mater. Chem. A*, 2013, **1**, 1141-1147.
4. X. Yang, K. Fan, Y. Zhu, J. Shen, X. Jiang, P. Zhao and C. Li, *J. Mater. Chem.*, 2012, **22**, 17278-17283.
5. H.-X. Zhang, C. Feng, Y.-C. Zhai, K.-L. Jiang, Q.-Q. Li and S.-S. Fan, *Adv. Mater.*, 2009, **21**, 2299-2304.
6. A. C. O'Sullivan, *Cellulose*, 1997, **4**, 173-207.
7. L.-F. Chen, Z.-H. Huang, H.-W. Liang, H.-L. Gao and S.-H. Yu, *Adv. Funct. Mater.*, 2014, **24**, 5104-5111.
8. S. K. Hoekman, A. Broch and C. Robbins, *Energy Fuels*, 2011, **25**, 1802-1810.
9. D. Roy, M. Semsarilar, J. T. Guthrie and S. Perrier, *Chem. Soc. Rev.*, 2009, **38**, 2046-2064.
10. M. N. Nadagouda and R. S. Varma, *Biomacromolecules*, 2007, **8**, 2762-2767.
11. D. Li, C. Lv, L. Liu, Y. Xia, X. She, S. Guo and D. Yang, *ACS Cent. Sci.*, 2015, **1**, 261-269.
12. W. Zhao, P. Yuan, X. She, Y. Xia, S. Komarneni, K. Xi, Y. Che, X. Yao and D. Yang, *J. Mater. Chem. A*, 2015, **3**, 14188-14194.
13. D. Li, D. Yang, X. Zhu, D. Jing, Y. Xia, Q. Ji, R. Cai, H. Li and Y. Che, *J. Mater. Chem. A*, 2014, **2**, 18761-18766.
14. X. Yang, K. Fan, Y. Zhu, J. Shen, X. Jiang, P. Zhao, S. Luan and C. Li, *ACS Appl. Mater. Interfaces*, 2013, **5**, 997-1002.
15. Y. Wang, F. Yan, S. W. Liu, A. Y. S. Tan, H. Song, X. W. Sun and H. Y. Yang, *J. Mater. Chem. A*, 2013, **1**, 5212-5216.
16. C.-W. Kim, D.-S. Kim, S.-Y. Kang, M. Marquez and Y. L. Joo, *Polymer*, 2006, **47**, 5097-5107.
17. C. Liu and R. Bai, *J. Membr. Sci.*, 2005, **267**, 68-77.
18. C. S. R. Freire, A. J. D. Silvestre, C. P. Neto, M. N. Belgacem and A. Gandini, *J. Appl. Polym. Sci.*, 2006, **100**, 1093-1102.
19. J. Liu, T. Yang, D.-W. Wang, G. Q. M. Lu, D. Zhao and S. Z. Qiao, *Nat. Comm.*, 2013, **4**, 2798.
20. J. Tang, J. Liu, N. L. Torad, T. Kimura and Y. Yamauchi, *Nano Today*, 2014, **9**, 305-323.
21. J. Liu, N. P. Wickramaratne, S. Z. Qiao and M. Jaroniec, *Nat. Mater.*, 2015, **14**, 763-774.
22. D. Liu, X. Wang, X. Wang, W. Tian, Y. Bando and D. Golberg, *Sci. Rep.*, 2013, **3**, 2543.
23. X. Wang, D. Liu, Q. Weng, J. Liu, Q. Liang and C. Zhang, *NPG Asia Mater.*, 2015, **7**, e171.
24. G. Zhou, L. Li, Q. Zhang, N. Li and F. Li, *Phys. Chem. Chem. Phys.*, 2013, **15**, 5582-5587.
25. L. Wang, B. Liu, S. Ran, H. Huang, X. Wang, B. Liang, D. Chen and G. Shen, *J. Mater. Chem.*, 2012, **22**, 23541-23546.
26. H. Guan, X. Wang, S. Chen, Y. Bando and D. Golberg, *Chem. Commun.*, 2011, **47**, 12098-12100.
27. X. Wang, W. Tian, D. Liu, C. Zhi, Y. Bando and D. Golberg, *Nano Energy*, 2013, **2**, 257-267.
28. X. Wang, Q. Weng, X. Liu, X. Wang, D. M. Tang, W. Tian, C. Zhang, W. Yi, D. Liu, Y. Bando and D. Golberg, *Nano Lett.*, 2014, **14**, 1164-1171.

